



ELSEVIER

Available online at www.sciencedirect.com

SCIENCE @ DIRECT®

Journal of Magnetism and Magnetic Materials 293 (2005) 597–604



www.elsevier.com/locate/jmmm

Magnetic separation in microfluidic systems using microfabricated electromagnets—experiments and simulations

Kristian Smistrup*, Ole Hansen, Henrik Bruus, Mikkel F. Hansen

MIC—Department of Micro and Nanotechnology, Technical University of Denmark, DTU - Building 345 East, DK-2800 Kongens Lyngby, Denmark

Available online 7 March 2005

Abstract

We present experiments and simulations of magnetic separation of magnetic beads in a microfluidic channel. The separation is obtained by microfabricated electromagnets. The results of our simulations using FEMLAB and Mathematica are compared with experimental results obtained using our own microfabricated systems.

© 2005 Elsevier B.V. All rights reserved.

Keywords: Microsystems; Magnetic separation; Computational fluid dynamics; Magnetophoresis; FEMLAB software; Microfluidics; Simulation; Electromagnet; Microelectromagnet; Nanotechnology; Channel flow

1. Introduction

Manipulation of superparamagnetic nanoparticles encapsulated in polymer beads (magnetic beads) is a well-known technique in biochemical analysis and processing [1,2]. In magnetic separation biochemically functionalized magnetic beads are separated from a solution using magnetic forces. Recently, microsystems offering the same functionality have been reported [3–5]. Microsystems capable of magnetic separation are ideal for inclusion in Lab-on-a-chip systems. The vision of Lab-on-a-chip systems is to have entire biochemical

laboratories on a single chip. The advantages of such Lab-on-a-chip systems are that they can handle minute sample volumes (e.g. micro or nanolitres), they are highly portable, and they are potentially inexpensive and thus disposable [6,7].

We present numerical simulations of the movements of such magnetic beads in microfluidic systems and compare with experiments.

2. Design and fabrication

The design of our microsystem is shown in Fig. 1. Each microsystem contains three micro-electromagnets, each consisting of a copper coil semi-encapsulated in a dielectric layer and a nickel soft magnetic yoke on top of that.

*Corresponding author. Tel.: +45 4525 5753; fax: +45 4588 7762.

E-mail address: krs@mic.dtu.dk (K. Smistrup).

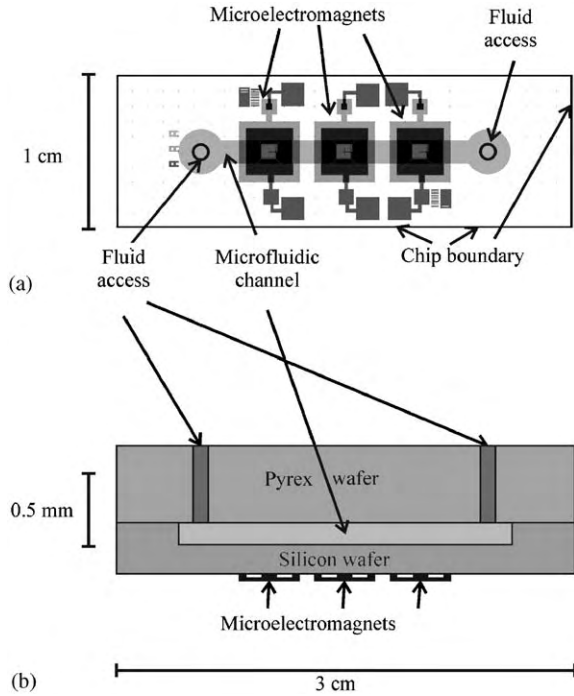


Fig. 1. Overview of the microsystem design. (a) Top-view of the fabricated chip. The microelectromagnets are planar spiral copper coils with 12 turns. The coils are semi-encapsulated in a soft magnetic yoke made from nickel. (b) The microsystem seen from the side. The horizontal scale bar at the bottom applies to both (a) and (b).

We have fabricated electromagnets by use of standard cleanroom technology. Fig. 2 summarizes the fabrication process. For more details see Ref. [8]. The electromagnets that we have used for the experimental part of this paper have the following design parameters: number of turns 12; coil wire height $25\ \mu\text{m}$, width $60\ \mu\text{m}$, and spacing $20\ \mu\text{m}$; electromagnet width $4\ \text{mm}$, and yoke thickness $25\ \mu\text{m}$; fluid channel depth $150\ \mu\text{m}$, length $14\ \text{mm}$, and width $1.5\ \text{mm}$.

3. Magnetostatic theory

The magnetic induction \mathbf{B} is calculated using magnetostatics formulae,

$$\mathbf{B} = \nabla \times \mathbf{A} = \mu_0 \mu_r \mathbf{H}, \quad (1)$$

$$\nabla \times \mathbf{H} = \mathbf{J}^f, \quad (2)$$

where \mathbf{H} is the magnetic field, \mathbf{A} is the magnetic vector potential, μ_0 is the permeability of vacuum, μ_r is the relative permeability of the material, and \mathbf{J}^f is the free current density. These equations can be combined to yield

$$\nabla \times ((\mu_0 \mu_r)^{-1} (\nabla \times \mathbf{A})) = \mathbf{J}^f. \quad (3)$$

To simplify the simulations we study circular electromagnets, and thus the magnetostatic problem is reduced from 3D to 2D. This still allows for qualitative comparison with the square magnets of the experiments as discussed by Shafique et al. [9].

We apply cylindrical coordinates (r, θ, z) with $r = 0$ at the centre of the electromagnet. All free currents are thus in the azimuthal direction $\mathbf{J}^f = J^f(r, z) \hat{\mathbf{e}}_\theta$ which is consistent with a magnetic vector potential $\mathbf{A} = A_\theta(r, z) \hat{\mathbf{e}}_\theta$.

To bring Eq. (3) into a form suitable for the software, FEMLAB[®], we introduce the function $u(r, z)$ given by

$$u(r, z) = \frac{A_\theta(r, z)}{r}. \quad (4)$$

Using this, the only non-zero component of Eq. (3) is

$$-\frac{\partial}{\partial r} \left(r(\mu_0 \mu_r)^{-1} \frac{\partial u}{\partial r} + 2(\mu_0 \mu_r)^{-1} u \right) - \frac{\partial}{\partial z} \left(r(\mu_0 \mu_r)^{-1} \frac{\partial u}{\partial z} \right) = J_\theta^f, \quad (5)$$

which is the canonical form that FEMLAB[®] solves in its ‘‘Magnetostatics–Azimuthal currents’’ mode of its Electromagnetics Module [10]. In terms of $u(r, z)$ the components of the magnetic induction become:

$$\mathbf{B} = (B_r, B_\theta, B_z) = \left(-r \frac{\partial u}{\partial z}, 0, r \frac{\partial u}{\partial r} + 2u \right). \quad (6)$$

Nickel is a ferromagnetic material, and thus μ_r is not a constant. However, since nickel is a soft magnetic material and thus almost hysteresis-free, we use the approximate empirical Fröhlich–Kennelly relation $\mathbf{M} = M_s \mathbf{H} / (C + |\mathbf{H}|)$ for hysteresis-free magnetization to describe the material [11].

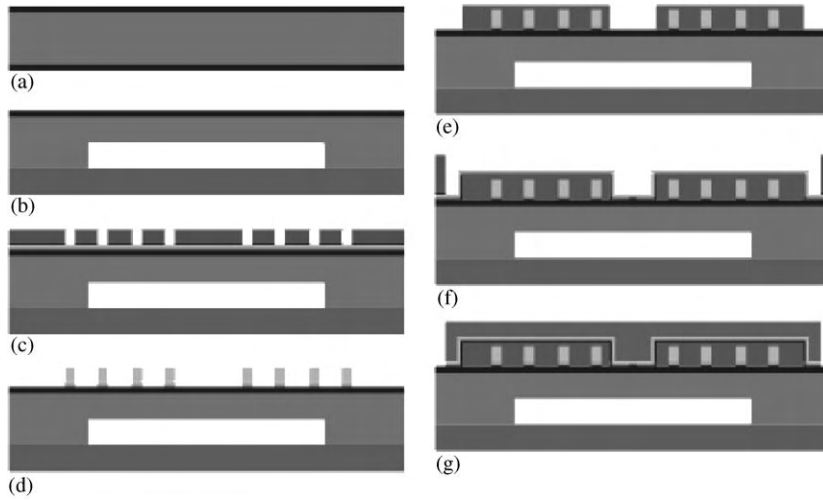


Fig. 2. Process flow for the fabrication of a micromachined magnetic bead separator. (a) A double polished silicon wafer is oxidized (50 nm) and 100 nm silicon nitride is grown. (b) The microfluidic channel (150 μm deep) is etched using deep reactive ion etching (DRIE), and a pyrex lid is attached by anodic bonding. (c) A seed layer is deposited, and a 25 μm layer of photoresist (AZ4562 from Hoechst is used throughout) is spun onto the wafer and patterned using UV-lithography. (d) The copper wire is electroplated into the resist mould followed by resist and seed layer removal. (e) A patterned layer of hard-baked photoresist forms the dielectric layer. (f) A seed layer is deposited and a new photoresist mould is defined. (g) A 25 μm nickel magnetic yoke is electroplated into the resist openings. Finally the resist and seed layer are removed.

The relative permeability $\mu_r(\mathbf{H})$ thus becomes

$$\mu_r(\mathbf{H}) = 1 + \frac{M_s}{C + |\mathbf{H}|}, \quad (7)$$

where M_s is the saturation magnetization of the material, and C is an experimentally determined parameter.

In order to solve Eq. (5) in FEMLAB[®], it is necessary to express μ_r as a function of \mathbf{B} (or actually as a function of u and its partial derivatives) rather than \mathbf{H} in order to use it in Eq. (5). By setting $|\mathbf{H}| = |\mathbf{B}|/\mu_0\mu_r$ in Eq. (7), μ_r is found as the positive root of a second order polynomial, which to first order in $|\mathbf{B}|$ is

$$\mu_r(|\mathbf{B}|) = 1 + \frac{M_s}{C} - \frac{M_s}{C(C + M_s)} \frac{|\mathbf{B}|}{\mu_0} + O(|\mathbf{B}|^2). \quad (8)$$

It is seen that $\mu_r(|\mathbf{B}|)$ is constant until the magnetic field inside the magnetic material approaches the saturation magnetization (assuming $M_s \gg C$).

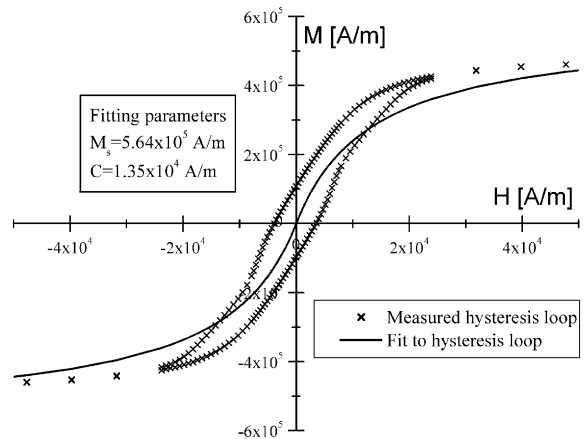


Fig. 3. \mathbf{M} vs. \mathbf{H} loop of an electroplated nickel film. The measured saturation magnetization is 4.84×10^5 A/m. The line is the fitted Fröhlich–Kennelly relation described in the text.

Fig. 3 features the measured hysteresis loop of one of our electroplated nickel thin films together with a fit based on Eq. (7). We have focused on a good fit for the low-field part of the hysteresis loop, which is why we have allowed for a saturation magnetization in the fit, which is

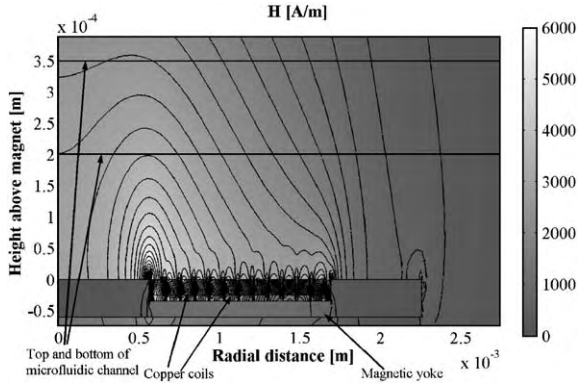


Fig. 4. Contour plot of the magnitude of the calculated \mathbf{H} -field. The current in the copper coil is 360 mA. Also shown is the position of the microfluidic channel relative to the electro-magnet. The magnetic beads will be attracted to regions where the magnetic field is large.

different from the nickel saturation magnetization of 4.84×10^5 A/m.

We have used the electromagnetics module of FEMLAB[®] 2.3 to solve Eqs. (4) through (7) with the parameters of the electroplated nickel thin film. In order to keep the magnetic reluctance of the entire system constant, all length scales have been scaled in order to have the same area in the circular geometry as in the original square geometry [9]. This yields a scaling factor of $(4/\pi)^{1/2}$. The free current density has been scaled with the inverse factor to ensure that the total current is unchanged.

Fig. 4 shows the result of such a calculation. Note that the magnetic beads will be attracted to areas in the microfluidic channel with large magnetic field and thus the attraction will be perpendicular to the contours of Fig. 4 (since these are also contours of $|\mathbf{H}|^2$). The fact that $|\mathbf{H}|$ inside the magnetic yoke does not exceed 2000 A/m, means that μ_r is everywhere within 80% of the constant $1 + M_s/C$ in Eq. (8).

4. Magnetic force on a magnetic bead

First, the magnetic force on a magnetic bead is calculated from the calculated magnetic field. The general expression for the magnetic force on a

magnetizable object is given by [12]

$$\mathbf{F}_{\text{mag}} = \mu_0 \int_V (\mathbf{M} \cdot \nabla) \mathbf{H}_a d^3r, \quad (9)$$

where the integral is taken over the volume of the magnetizable object, and \mathbf{H}_a is the magnetic field in the absence of the magnetizable object.

For a spherical bead in a homogeneous magnetizing field, the magnetization \mathbf{M} inside the bead is given by [13]

$$\mathbf{M} = \chi_m \mathbf{H}_a = \frac{\chi_i}{1 + N\chi_i} \mathbf{H}_a = 3 \frac{\mu_r - 1}{\mu_r + 2} \mathbf{H}_a, \quad (10)$$

where χ_i is the intrinsic susceptibility of the magnetic bead material, χ_m is the measured susceptibility of a single magnetic bead including demagnetization effects, and $\mu_r = 1 + \chi_i$ is the relative permeability of the magnetic bead material. It has been assumed that the sphere is surrounded by a medium with $\chi \approx 0$. The last equality follows from the fact that the demagnetization factor of a sphere is $N = \frac{1}{3}$. At this point it is not necessary to assume that χ is constant; however, this assumption simplifies the following equations substantially, and is justified for the fields inside the microfluidic channel in our case. Inserting this into Eq. (9) and taking the magnetizable object to be a magnetic bead yields:

$$\begin{aligned} \mathbf{F}_{\text{mag}} &= \mu_0 3 \frac{\mu_r - 1}{\mu_r + 2} \int_{\text{Bead}} (\mathbf{H}_a \cdot \nabla) \mathbf{H}_a d^3r \\ &\approx 2\pi R^3 \mu_0 \frac{\mu_r - 1}{\mu_r + 2} \nabla(|\mathbf{H}_a|^2) \\ &= \frac{1}{2} \mu_0 V_{\text{bead}} \chi_m \nabla(|\mathbf{H}_a|^2). \end{aligned} \quad (11)$$

The approximation is that the integrand is constant over the volume V_{bead} of a magnetic bead with radius R , and it has been used that \mathbf{H}_a is curl-free, since there are no free currents outside the copper coils. This result is consistent with the effective dipole approximation reported by Jones [14], but it has been found through different means.

5. Dynamics and microfluidic theory

Low Reynolds numbers and hence laminar flows generally characterize fluid flows in

microfluidic systems. For example in our system and for the used flow rates the Reynolds number is approximately 10^{-2} , and thus all inertial terms in the Navier–Stokes equation can be discarded. Since we are considering stationary incompressible flow in straight channels with no net body force on the fluid, the Navier–Stokes equation reduces to:

$$\left(\frac{\partial^2}{\partial y^2} + \frac{\partial^2}{\partial z^2}\right)v_x(y, z) = -\frac{\Delta p}{\eta L}, \quad (12)$$

where Δp is the pressure drop across the length L of the microfluidic channel, η is the viscosity of the fluid, and $v_x(y, z)$ is the longitudinal velocity in the channel. Using the usual no-slip boundary conditions on the walls $(y, z) \in [0, y_0] \times [0, z_0]$ the solution to Eq. (12) can be written as

$$v_x(y, z) = v_{\text{avr}} \frac{\phi(y, z)}{\langle \phi \rangle}, \quad (13)$$

$$\phi(y, z) = \sum_{n=0}^{\infty} f_n(z) \sin(k_n y), \quad k_n = (2n + 1) \frac{\pi}{y_0}, \quad (14)$$

$$f_n(z) = \frac{-1}{(2n + 1)^3} \left(\cosh(k_n z) - \tanh\left(k_n \frac{z_0}{2}\right) \sinh(k_n z) - 1 \right), \quad (15)$$

$$\langle \phi \rangle = \frac{1}{y_0 z_0} \int_0^{z_0} \int_0^{y_0} \phi(y, z) dy dz, \quad (16)$$

where v_{avr} is the average flow velocity in the channel given by $v_{\text{avr}} = Q/y_0 z_0$ where Q is the volumetric flow rate. In experimental microfluidics the flow rate is often the adjustable parameter rather than the pressure difference, and the solution is expressed in terms of Q . For the numerical calculations, the sum in Eq. (14) was truncated at $n = 100$.

We take the fluid drag on a magnetic bead to be the Stokes drag:

$$\mathbf{F}_{\text{fluid}} = 6\pi R\eta(\mathbf{v}_{\text{fluid}} - \mathbf{v}), \quad (17)$$

where η is the viscosity of the fluid, and $\mathbf{v}_{\text{fluid}}$ and \mathbf{v} are the velocity vectors of the fluid and bead, respectively.

Finally gravity is included through a buoyancy term:

$$\mathbf{F}_{\text{grav}} = \frac{4}{3}\pi R^3(\rho_{\text{fluid}} - \rho)g\hat{\mathbf{z}}, \quad (18)$$

where the ρ_{fluid} and ρ are the densities of the fluid and bead, respectively.

At this point we have accounted for all the forces that affect a magnetic bead in the fluid, and thus Newton's second law yields:

$$\rho \frac{4}{3} \pi R^3 \frac{d\mathbf{v}}{dt} = \mathbf{F}_{\text{mag}}(\mathbf{r}) + \mathbf{F}_{\text{grav}}(\mathbf{r}) + \mathbf{F}_{\text{fluid}}(\mathbf{r}, \mathbf{v}). \quad (19)$$

At a given bead position all forces can be considered constant except for $\mathbf{F}_{\text{fluid}}$ that depends on \mathbf{v} , and that yields a differential equation for \mathbf{v} with a solution that has a constant term (the equilibrium velocity) and a decaying exponential function with a time constant τ given by:

$$\tau = \frac{2R^2\rho}{9\eta} \approx 10^{-7} \text{ s}. \quad (20)$$

This shows that the bead reaches its equilibrium velocity, where all forces cancel, instantaneously compared to other time scales in the simulation, e.g. capture times, and thus it is justifiable to use the equilibrium velocity for calculations of the bead flows [15]. Hence we neglect the inertial term of Eq. (19), and obtain

$$\mathbf{v} = \frac{d\mathbf{r}}{dt} = \mathbf{v}_{\text{fluid}}(\mathbf{r}) + \frac{1}{6\pi R\eta}(\mathbf{F}_{\text{mag}}(\mathbf{r}) + \mathbf{F}_{\text{grav}}(\mathbf{r})). \quad (21)$$

Eq. (21) constitutes three coupled, first-order, ordinary differential equations of motion for the bead.

From the equations of motion it is seen that the largest magnetic forces appear in regions with the largest gradients in $|\mathbf{H}|^2$. Once caught by the magnetic gradient force, the particles are brought towards the local magnetic field maximum. Hence, we expect a high capture efficiency near such points, i.e. near edges and corners of magnetic structures.

6. Simulations

For the simulations we have used the parameters of the bead type MyOne[®] from Dynal Biotech [2], which are approximately: $2R = 1.05 \mu\text{m}$, $\rho = 1.8 \times 10^3 \text{ kg/m}^3$, and $\mu_r = 2.5$. Also, the permeability of the magnetic beads can be assumed constant, since the applied fields do not saturate the beads. The fluid is water with $\rho = 1.0 \times 10^3 \text{ kg/m}^3$ and $\eta = 8.90 \times 10^{-4} \text{ Pa s}$.

We have solved Eq. (21) using the numerical solver NDSolve of Mathematica[®] for many different initial positions of the magnetic beads. We have assumed that whenever a bead hits the bottom of the microfluidic channel, it sticks without any possibility of further motion.

Fig. 5 shows the result of a calculation where 10,000 magnetic beads have been released into the microfluidic channel from the left at equally spaced points. The flow rate is $1 \mu\text{L/min}$. From Fig. 5(a) it is noticed that many beads settle near the entrance of the channel. This is due to the low velocity of beads that are released very close to the bottom of the microfluidic channel so that gravity will have a large effect over short distances. However, since the fluid velocity near the bottom of the channel is small, the bead in-flux is also small there. In other words, the in-flux of magnetic beads is low for $z \approx 0$, whereas the in-flux is large for $z \approx z_0/2$. This is reflected in Fig. 5(b) that shows the bead settling probability density across the microfluidic channel. Each of the settling

points from Fig. 5(a) has been scaled with the fluid velocity at the entry point of the bead, since the in-flux of magnetic beads at an entry point is proportional to the fluid velocity at that entry point, if the bead concentration in the fluid is constant. Since the in-flux of magnetic beads in the part of the channel entrance (near the bottom of the channel) that would lead to settling points in the beginning of the channel is low, the settling probability density is not as high in the left part of the channel as might be expected from Fig. 5(a). It is Fig. 5(b) rather than Fig. 5(a) that one would expect to observe experimentally.

The most important feature of Fig. 5 is that the beads clearly tend to settle near the inner pole piece edges of the electromagnets, i.e., where the magnetic field is largest according to Fig. 4. This means that an experimentally observed bead-settling pattern would be expected to concentrate in these areas.

Fig. 6 shows a magnetic capture diagram of the entrance of the microfluidic channel, and it shows where beads with different initial positions settle in the microfluidic channel. It is seen how beads released near the sides or bottom of the microfluidic channel are more easily captured in the channel, since the fluid velocity at the release point is small, and thus both gravity and magnetic force will be large compared to the fluid drag. Fig. 6 also allows us to calculate the bead capture efficiency for the microsystem. It is simply the summed probabilities for bead entrance at all the different

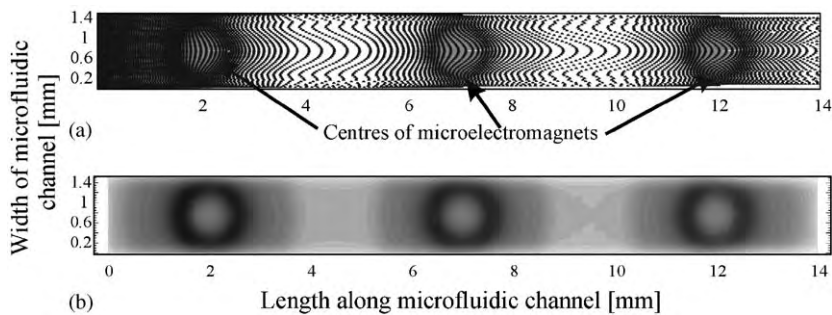


Fig. 5. Calculation of the trajectories of 10,000 magnetic beads, whose initial positions were equally spaced across the left entrance of the microfluidic channel. Each cross in the figure corresponds to a point, where a magnetic bead has settled. In (b) the settling points have been transformed into a settling probability density. The dark parts of the plot correspond to places with high settling probability density.

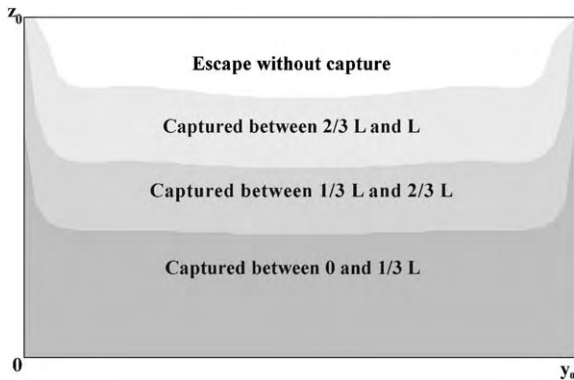


Fig. 6. The plot shows the fluid and bead entrance of the microfluidic channel, which has been divided into four areas corresponding to the position where a bead that started in that phase settled in the microfluidic channel, or if the bead escaped capture. L is the length of the microfluidic channel.

points in the entrance of the microfluidic channel that correspond to caught beads. In this case the capture efficiency is $\sim 89\%$.

7. Experiments

We have performed bead capture experiments using the described microfabricated system. While it is difficult to measure bead capture efficiencies and almost impossible to study bead trajectories when the dimensions of the microfluidic channel are large compared to the bead diameter, the bead-settling pattern is more easily observed. In the experiments we have used bead concentrations that are large enough to capture a significant number of magnetic beads, but still low enough that interactions between the magnetic beads in the solution are negligible.

Fig. 7 shows the bead-settling pattern of such an experiment. The picture is taken after 20 min, and it is seen how the beads have settled near the edges of the inner pole region of the square microelectromagnet. Beads captured along the edges are vaguely seen, but most beads have settled near the corners of the square electromagnet. As the simulations have been carried out for cylindrical electromagnets, the bead accumulation near corners is not predicted. However, the magnetic field is expected to be even more concentrated near the

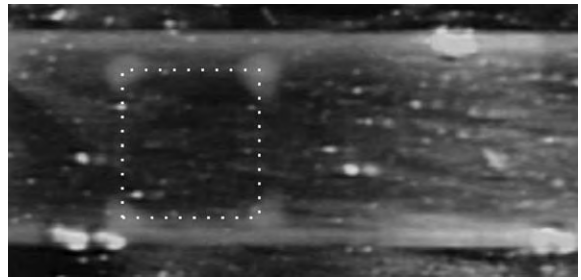


Fig. 7. Micrograph of captured beads on top of one microelectromagnet. The dotted square marks the inner pole of the electromagnet and has a side length of 1 mm. The magnetic beads are seen as the bright areas along the edge and close to the corners of the inner pole region of the electromagnets.

corners of the electromagnet, so when beads approach the bottom of the microfluidic channels, they will experience a horizontal force towards the corners. Also in the simulations the beads were supposed to stick, when they hit the bottom. Experimentally they might move along the bottom of the microfluidic channel, giving rise to the very high density of captured magnetic beads at the corners.

8. Conclusion

We have presented a simulation scheme for the movement and capture efficiency of magnetic beads in a microfluidic channel. Furthermore we have shown that the results of the simulations are in qualitative agreement with experimental data.

In the simulation scheme, we have neglected the effect of hydrodynamic and magnetic interactions between magnetic beads, and interactions between beads and channel walls. These effects are discussed in Ref. [16]. Also the movement of magnetic beads after they first hit the channel bottom has been neglected.

In Ref. [15] another simulation scheme is presented, where the local concentration of magnetic beads in the fluid is treated as a continuous function, and the behaviour of the local bead concentration as a function of time is discussed. In that scheme it is also found that the beads move towards regions with large magnetic field, so there is a qualitative agreement between that simulation

scheme and the one presented here, where the movement of single magnetic beads are considered.

References

- [1] J.H.P. Watson, *J. Appl. Phys.* 44 (1973) 4209.
- [2] Dynal BioTech, www.dynabead.com.
- [3] C.H. Ahn, M.G. Allen, W. Trimmer, et al., *J. Microelectromech. Syst.* 5 (1996) 151.
- [4] J.W. Choi, T.M. Liakopoulos, C.H. Ahn, *Biosens. Bioelectron.* 16 (2001) 409.
- [5] T. Deng, M. Prentiss, G.M. Whitesides, *Appl. Phys. Lett.* 80 (2002) 461.
- [6] J. Knight, *Nature* 418 (2002) 474.
- [7] B.H. Weigl, R.L. Bardell, C.R. Cabrera, *Adv. Drug Del. Rev.* 55 (2003) 349.
- [8] K. Smistrup, O. Hansen, P.T. Tang, et al., Lab-on-a-Chip, submitted.
- [9] M. Shafique and M.F. Hansen, Proceedings of the Nordic Matlab Conference, 2003, p. 209.
- [10] Documentation manual for FEMLAB[®] 2.3, www.femlab.com.
- [11] D. Jiles, *Introduction to Magnetism and Magnetic Materials*, second ed., Chapman & Hall, ISBN 0-412-79860-3, 1998, pp. 115–117.
- [12] A. Engel, R. Friedrichs, *Am. J. Phys.* 70 (2002) 428.
- [13] R.C. O’Handley, *Modern Magnetic Materials—Principles and Applications*, Wiley, New York, ISBN 0-471-15566-7, 2000, pp. 38–47.
- [14] T.B. Jones, *Electromechanics of Particles*, Cambridge University Press, ISBN 0-521-43196-4, 1995.
- [15] K.C. Warnke, *IEEE Trans. Magn.* 39 (2003) 1771.
- [16] C. Mikkelsen, M.F. Hansen, H. Bruus, *J. Magn. Magn. Mater.* (2005), this issue.